JOURNAL OF MATERIALS SCIENCE **38** (2003) 2117–2123

Micro-mechanisms, mechanical behaviour and probabilistic fracture analysis of PA 66 fibres

A. MARCELLAN, A. R. BUNSELL, R. PIQUES
Ecole des Mines de Paris, Centre des Matériaux, 91003 Evry Cedex, France
E-mail: alba.marcellan@mat.ensmp.fr

Ph. COLOMBAN
LADIR, UMR 7075 CNRS-UPMC, 2 rue Henry-Dunant, 94320 Thiais, France

The micro/macro structural evolution of polyamide 66 fibres during tensile loading and failure initiation have been studied by coupling multi-scale measurements such as wide angle X-ray diffraction (WAXD) with profile fitting, birefringence, differential scanning calorimetry (DSC), micro-Raman spectroscopy and mechanical testing at two strain rates. A large dependence of mechanical properties, including strain rate effects, on the behaviour of both oriented and random amorphous regions has been shown with important contributions from the isotropic amorphous domains. The results indicate the presence of compressive residual stresses beneath the skin, showing a skin/core sub-structure. Statistical fracture treatments have been applied using a time-dependent weakest link Weibull model, in order to give an evaluation of the dispersion of defects. Local damage was taken into account using a crack growth propagation law as a function of stress intensity factor near the defect. The paper shows how both experimental and theoretical fracture toughness results are in quite good agreement. © *2003 Kluwer Academic Publishers*

1. Introduction

The present work concerns yarns commercialised by Rhodia (France). Two are used for tyre reinforcement and one for textile applications. The study attempts to reveal the relationship between the microstructure of the fibres and their mechanical behaviour (i.e., uniaxial loading and fracture toughness) and to reveal the mechanisms responsible for tensile crack initiation.

Macroscopic mechanisms of failure have been revealed by scanning electron microscopy (SEM). The cracks initiate at the surface or in the skin of the fibre. The identification of the microstructural processes responsible for final failure represents the main challenge for this study. Multi-scale analyses were coupled with a mechanical study and a probabilistic fracture analysis in order to obtain an accurate description of mechanisms during loading and failure.

2. Experimental procedure

2.1. Materials

Three commercial yarns of PA 66 ($\varnothing \sim 30\ \mu$m) have been studied. Two were high performance and ultra-high performance multifilaments, respectively labelled A and B, both used for tyre reinforcement. Fibres labelled C, containing TiO_2 powder possessed lower mechanical properties than the other two types of fibre and were destined for textile applications. Comparative microstructural analyses were performed on these 3 samples in order to better understand the effects of microstructural parameters on mechanical behaviour and fracture toughness.

2.2. Wide angle X-ray diffraction (WAXD)

θ-2θ WAXD scans were obtained using a Siemens D500 diffractometer in the transmission mode using Co K_α radiation ($\lambda = 1.789$ Å), with a linear detector (Elphyse). Yarns were mounted on a sample holder to maintain the filaments parallel to one another (samples were submitted to different strain levels). The scans were collected between $2\theta = 15°$ and $40°$. θ-2θ scans were obtained with the sample spinning in its own plane to determine the index of cristallinity and to evaluate orientation. A sequence of θ-2θ scans were carried out in the azimuthal angle range $\varphi(-5°$ to $90°$, with azimuthal increments from 2.5° to 5°). Equatorial scans, conventionally $\varphi = 0°$, were obtained to determine phase proportions and apparent crystallite sizes (ACS). The θ-2θ scans obtained at various azimuthal angles were resolved into crystalline and amorphous contributions using a profile fitting program based on the least-square procedure. The background was supposed linear. Pearson VII functions (Equation 1) were used, as has been described elsewhere in the bibliography [1, 2]:

$$I(x) = \frac{I_o}{\left(1 + 4\left(\frac{x - x_o}{\text{fwhm}}\right)^2 (2^{1/m} - 1)\right)^m} \tag{1}$$

Shape factors m were fixed at 2 for all peaks. Full width at half-maxima (fwhm) variations were interpreted as a measure of crystallite size. Crystalline peaks, respectively (100) and (010) + (110) were maintained fixed after optimisation of their position in an equatorial scan.

The θ-2θ scans of sample B were recorded at different levels of strain: 0%–5% & 10%.

The parameters of the amorphous and crystalline peaks were plotted as a function of azimuthal angle φ, in order to determine the different microstructural characteristics.

2.3. Micro-Raman spectroscopy

Raman spectra were obtained using a Dilor 'XY' spectrometer (Lille, France) with double holographic monochromator and a X-Y micrometric plate allowing 2D displacements. The source was an Ar^+-Kr^+ ion laser (model 'Innova 70', Coherent), used at a wavelength of 647.1 nm and a power of 15 mW (at the sample). Aperture slits were about 60 μm. Excitation and collection were performed with an Olympus optical microscope ($\times 1000$). Detection was ensured by a high sensitive nitrogen-cooled charge coupled (CCD) camera (model 'Spex' 2000 × 250 pixels with backside illumination), giving a resolution of 0.3 cm^{-1}. Low frequency modes have been investigated from 30 cm^{-1} to 500 cm^{-1}. Raman scans have been treated using mixed Lorentzian/Gaussian profile fitting in order to isolate the Rayleigh diffusion contribution on the spectra.

Single fibres were mounted in a 'Universal Fibre Tester' (see hereafter) device for different strain levels. Raman spectra obtained during mechanical loading were monitored after stabilisation of viscoelastic behaviour. Exposure times were about 2700 s. The laser was focused on fibre edges (spot size ~1 μm diameter) and was polarised either parallel to the fibre axis (noted //) or perpendicular (noted $\perp$).

2.4. Birefringence & differential scanning calorimetry (DSC)

Birefringence was measured on a Leitz polarising microscope using a Berek compensator. The amorphous orientation, f_{ab} , was determined by this method in comparison with the WAXD value. According to the expression [3]:

$$\Delta = n_{\perp} - n_{//} = \chi f_c \Delta_c^{\circ} + (1-\chi) f_{ab} \Delta_a^{\circ} \qquad (2)$$

in which Δ is the measured optical birefringence, χ is the crystallinity (in volume), f_c is the crystalline orientation, Δ_a° and Δ_c° are respectively the intrinsic optical birefringence of amorphous and crystalline domains. The value of f_{ab} was determined using $^{*}\Delta_a^{\circ} = 0.077$ and $\Delta_c^{\circ} = 0.096$ [4] (or also $^{**}\Delta_a^{\circ} = \Delta_c^{\circ} = 0.073$ [5]).

Crystallinity measurements were carried out using a 'TA Instruments 2920' DSC in order to compare with the WAXD evaluation. The ratio between the experimental melting enthalpy and the melting enthalpy of a perfect crystal gives the crystallinity Xc as follows:

$$Xc = \frac{\Delta H_{\text{exp}}}{\Delta H f^{\circ}} \qquad (3)$$

where $\Delta H_f^{\circ} = 196$ J/g [6].

Fibres were stored under controlled conditions (21°C and 50% R.H.). A heating rate of 10°C/min from room temperature to 330°C was applied to the samples ($\cong$5 mg crimped in aluminium pan).

2.5. Mechanical testing

The single fibres were tested under controlled conditions of temperature and relative humidity (21°C and 50%) with a Universal Fibre Tester, the details of which have been given elsewhere [7]. The loading was monitored with an accuracy of 0.1 g under tensile conditions. The specimen gauge length was 50 mm. Two strain rates were used 2.5×10^{-3} s^{-1} and 8.3×10^{-3} s^{-1} in order to study viscoelastic effects. Fibre diameters were systematically measured before tests.

3. Results and discussion

3.1. Mean characteristics of microstructure

θ-2θ WAXD scans were obtained for various azimuthal angles. Fig. 1 shows an example of a profile fitting of an equatorial pattern. Profile results of the θ-2θ scans were plotted Fig. 2 as a function of azimuthal angle for crystalline and amorphous contributions. Results are summarised in Table I. WAXD measurements coupled with

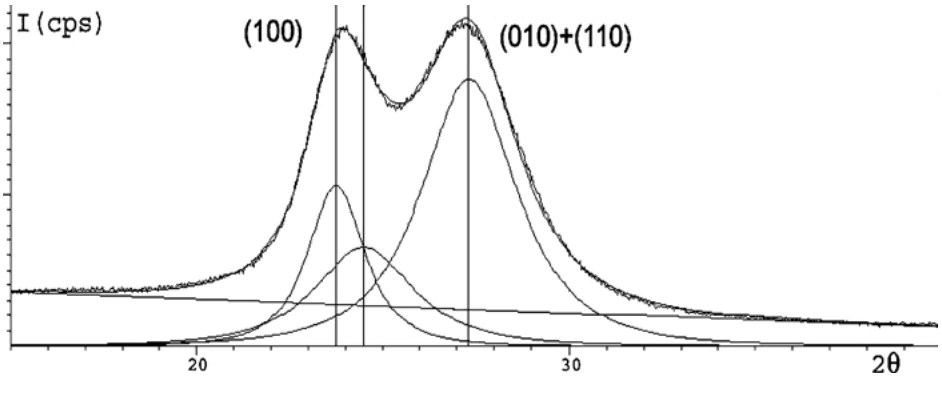

Figure 1 WAXD equatorial θ-2θ scan deconvoluated into amorphous and crystalline contributions (sample A).

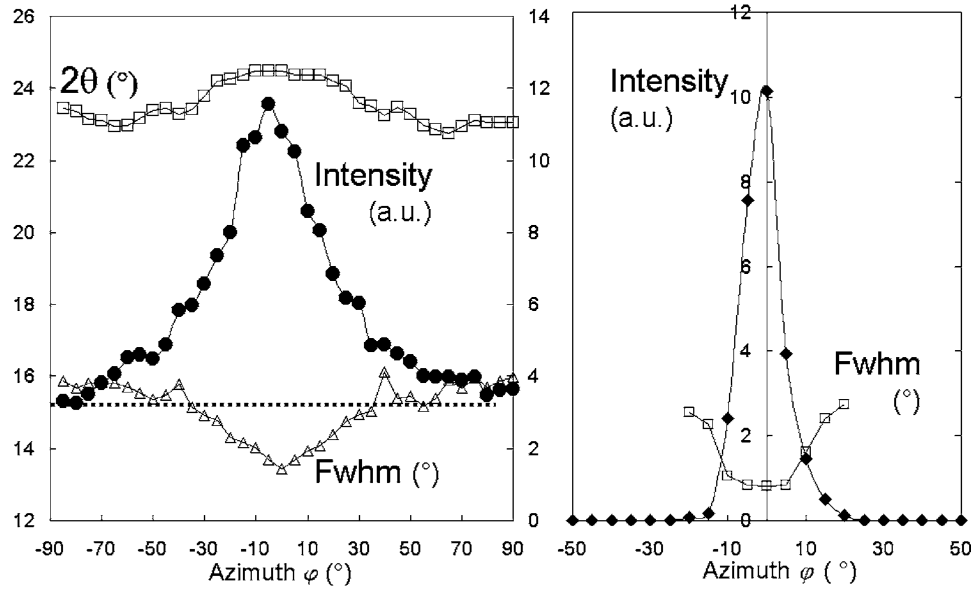

(a) (b)

Figure 2 WAXD peak parameter evolutions (a) for the amorphous domain, and (b) for (100) crystal planes (sample A).

profile fitting provide information at different scales: from the identification of phases, to the index of crystallinity, the ratio of oriented amorphous regions, the degree of orientation and including the crystallite sizes.

3.1.1. Phase identification

The α phase initially defined by Bunn and Garner [8] has been identified as the major phase in these fibres. Only traces of the β phase were observed at $2\theta \approx 12^\circ$ for (002) layers reflections, and no γ phase was seen.

The description of the triclinic unitary cell $\alpha(a = 4.9$ Å, $b = 5.4$ Å, $c = 17.2$ Å, $\alpha = 48.5^\circ$, $\beta = 77^\circ$, $\gamma = 63.5^\circ$, **c** along the chain axis [8]) has been refined into α_{I} and α_{II} phases [9]. α_{I} and α_{II} phases are described as slight variations of crystallographic parameters of the α phase, the α_{I} phase being more highly ordered than the α_{II} phase ($d_{\alpha\mathrm{I}} = 1.213\ \mathrm{g \cdot cm^{-3}}$ and $d_{\alpha\mathrm{II}} = 1.173\ \mathrm{g \cdot cm^{-3}}$ [10]).

Crystalline perfection, defined as $\Delta(\theta_{010+110} - \theta_{100})$, was evaluated for all samples in terms of the ratio of α_{I} and α_{II} phases, assuming that crystalline perfection was directly proportional to the theoretical crystalline perfection of α_{I} and α_{II} crystals ($\Delta\theta_{\alpha\mathrm{I}} = 105$ min, $\Delta\theta_{\alpha\mathrm{II}} = 25$ min, with Cu K_α radiation [9]). The α_{I} phase was largely predominant in all samples with C yarns which show slightly less α_{I} phase.

TABLE I Microstructural results (see text for symbol explanation)

Mechanical performance	**A** high performance	**B** ultra-high performance	**C** textile (+TiO_2)
α_{I}%	83	83	76
Xc%	39	46	45
Xoa%	20	23	13
Xia%	41	31	42
Foa	0.33	0.42	0.23
f_{c}	0.976	0.977	0.929
f_{am}	0.650	0.655	0.639
ACS_{100} (Å)	68	66	61
$\Delta(10^{-3})$	60.0	61.6	55.3
$f_{\mathrm{ab}^{*}-^{**}}$	0.536–0.736	0.485–0.744	0.408–0.637
Xc_{DSC}%	41	44	45

3.1.2. Identification of amorphous regions and index of crystallinity

The evolution of amorphous peak parameters shown in Fig. 2a such as intensity (peak area), fwhm and position reveal that part of the amorphous domain depends on orientation. Changes in the position of the amorphous halo, with a maximum value for equatorial scans show that this amorphous phase consists of denser oriented and less dense isotropic regions.

Xoa, index of oriented amorphous domain and *Xia*, index of isotropic amorphous domain were defined from peak intensity variations $I(\varphi)$ assuming that the isotropic amorphous component remained independent of the φ angle (under the baseline Fig. 2a). Quantification of the isotropic amorphous and oriented amorphous regions remain the prime interest of the WAXD measurements coupled with profile fitting. The fraction of amorphous phase which is oriented, *Foa*, was also defined. We note that *Xoa* and *Foa* represent a pertinent indicator highly correlated to the mechanical performance (cf. Table I).

The crystallinity index, Xc, was defined as the ratio between the intensity diffracted by crystalline regions and the total intensity diffracted integrated over the φ directions. Crystalline indexes showed a high degree of crystallisation for our samples, with fibres B and C near to the maximum of crystallinity. Values obtained are coherent and in good accordance with the DSC results, as it is shown Fig. 3, and support the profile fitting method.

In DSC thermograms we can note that no cold crystallisation or residual stress relaxation have been observed. Moreover, the melting behaviour of sample C

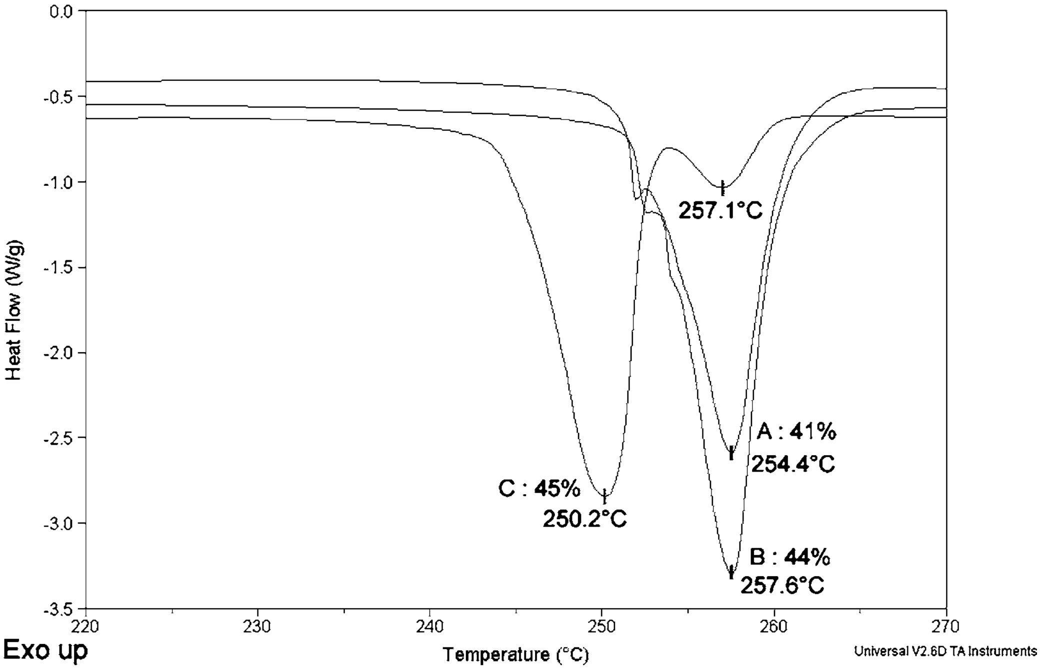

Figure 3 DSC thermograms at 10°C/min showing the melting behaviour in PA 66 fibres for samples A, B and C (sample size about 5 mg).

shows a large discrepancy compared to the other 2 samples, having a double melting peak. The presence of TiO_2 inclusions seems to have induced heterogeneous crystallisation by providing nucleation points and are responsible for this high value of crystallinity but certainly less ordered phases (cf. Orientation and ACS results).

3.1.3. Orientation degree of phases

In order to quantify the orientation of the crystalline and amorphous regions, analysis of the intensity as a function of azimuthal angle was performed, assuming a two phases model (cf. Fig. 2b).

The degree of orientation was calculated as the Hermans orientation factor [11]:

$$f_\phi = \frac{1}{2}(3\langle\cos^2\phi\rangle - 1) \tag{4}$$

with ϕ, the angle between normal of crystal planes diffracting and the reference fibre axis ($\phi = \pi/2 - \varphi$). The mean $\cos^2\phi$ was determined from the following expression, assuming rotational symmetry about the fibre axis:

$$\langle\cos^2\phi\rangle = \frac{\int_0^{\frac{\pi}{2}} I(\phi)\sin\phi\cos^2\phi\,\mathrm{d}\phi}{\int_0^{\frac{\pi}{2}} I(\phi)\sin\phi\,\mathrm{d}\phi} \tag{5}$$

with $I(\phi)$, diffracted intensity at ϕ. Plots were fitted with a gaussian peak shape. Hermans orientation factor being equal to 0 for a random distribution, 1 for a total alignment of the identities and $-1/2$ if all are perpendicular to the fibre axis.

This function was applied to calculate the orientation of the crystalline f_c and amorphous domains f_{am}, see Table I.

Crystalline domains of the 3 samples were seen to be parallel to the fibre axis and reached very high values of ordering (more than 0.9, cf. Table I). The amorphous phase was also oriented with values around 0.6.

The ultra-high performance sample (B) showed the highest values of orientation both in terms of crystalline (0.977) and amorphous regions (0.655), followed by sample A. The crystallisation of sample C shows less perfection with the minimum degree of orientation.

Birefringence measurements were in agreement with WAXD results with an identical order of global degree of orientation. The amorphous orientation function f_{ab}, has been evaluated using the birefringence value and introducing Xc and f_c provided by WAXD measurements. The results obtained have also confirmed the method of calculating f_{am}.

Selected area diffraction (about 3 μm diameter) by transmission electron microscope (TEM) has shown a random crystallite distribution around the **c** axis. No radial or ortho-radial texture has been seen.

3.1.4. Apparent crystallite size (ACS)

Profile analysis of equatorial scans was used to obtain an ACS in the normal direction of (hkl) layers using the Scherrer's formula [11]:

$$\mathrm{ACS_{hkl}} = \lambda/(\mathrm{fwhm}\cdot\cos\theta_{\mathrm{hkl}}) \tag{6}$$

In which λ is the wavelength, θ the peak position and fwhm the full-width at half-maximum of crystalline peak.

DSC was also able to give an indication of crystallite size or crystallite distortions based on T_f, the melting temperature. Thermograms Fig. 3 clearly show two melting behaviours interpreted in terms of two types of crystallite size distribution. Samples A and B contained an equivalent crystallite morphology with respect to a broad endothermic peak at ≅257.5°C, whereas sample C presented two well-defined melting peaks: an additional peak at the lower melting temperature ($T_f \cong 250.2°C$). Two sizes of crystallites or two types of crystalline perfection are identified with only about 10% of large crystallites (same morphology as A and B) and about 90% of the smallest. The additional TiO_2 introduced in sample C produced an heterogeneous crystalline growth involving high crystallinity, low ordering with distortions or smaller crystalline areas.

WAXD measurements only gave an average value for ACS. However WAXD results for equatorial scans are representative of this tendency with ACS_{100} about 67 Å for A and B and about 61 Å for C. Moreover, according to the fwhm evolution versus disorientation (fwhm minimum at equator), the larger crystallites seem to be oriented along the fibre axis during processing.

3.2. Gradient of property and damage localisation

Information at the scale of chemical bonds (0.1 to 1 nm) was provided by μ-Raman spectroscopy at various points with a resolution of the micron. The prime interest of the Raman spectrometry investigation was to obtain local information of the molecular conformation especially through of collective C—C skeletal motions at about 100 cm^{-1}. The vibrational response as shown in Fig. 4b was highly polarized and confirmed the high degree of crystallinity of the system. Raman spectroscopy has been used to follow C—C chain deformation during tensile loading. The suitability of the 100 cm^{-1} band for μ-Raman extensometry has been revealed with a large mechanical dependence on peak position of skeletal motions. Axial fibre calibration of the Raman wavenumber shift SR as a function of applied strain shows a threshold behaviour: C—C bonds are loaded only after 350 MPa stress, and then behave elastically ($\Delta\nu = -\mathrm{SR}\Delta\varepsilon$).

3.2.1. Skin/core effect

The evolution of peak position reveals the heterogeneity of the structure between the core and the skin of the fibre. A linear scanning measurements (line-scan) cartography across the fibre diameter (cf. Fig. 4a) with the laser focused on the fibre edges suggested the existence of residual compressive stresses in the skin (in the fibre axis direction), corresponding to a wavenumber shift between skin and core (skin wavenumber higher than that of the core).

These skin/core effects appeared to vary along the fibre. Rather than a simple skin/core effect it seems to be a gradient of properties due to the thermo-mechanical history seen by the first few micrometers near to the fibre surface during the processing. The value of the compressive residual stresses is evaluated at about 200 MPa from the calibration plot and is explained by a higher oriented zone in the skin (equivalent to a higher draw ratio).

In addition, fibre C showed a heterogeneous distribution of TiO_2 inclusions along the length of the fibre. The main Raman fingerprint of TiO_2 anatase peak arises at 143 cm^{-1}. Because of the presence of this latter peak, profile fitting became more complex and solutions found were more unreliable. It was consequently, difficult to identify such a skin/core effect in sample C.

TEM observations were also carried out in order to identify a skin/core effect, but no crystallographic changes were revealed. Sample preparation still remained the critical step for electron diffraction analysis.

3.2.2. Local damage zones

Fibres were submitted to different strain levels. Local damage was observed by optical confocal microscope imaging coupled with μ-Raman spectroscopy.

At a strain level of about 10%, various damaged zones appear along the fibre. Abnormal laser diffusion occurred at defects and so revealed them. Near

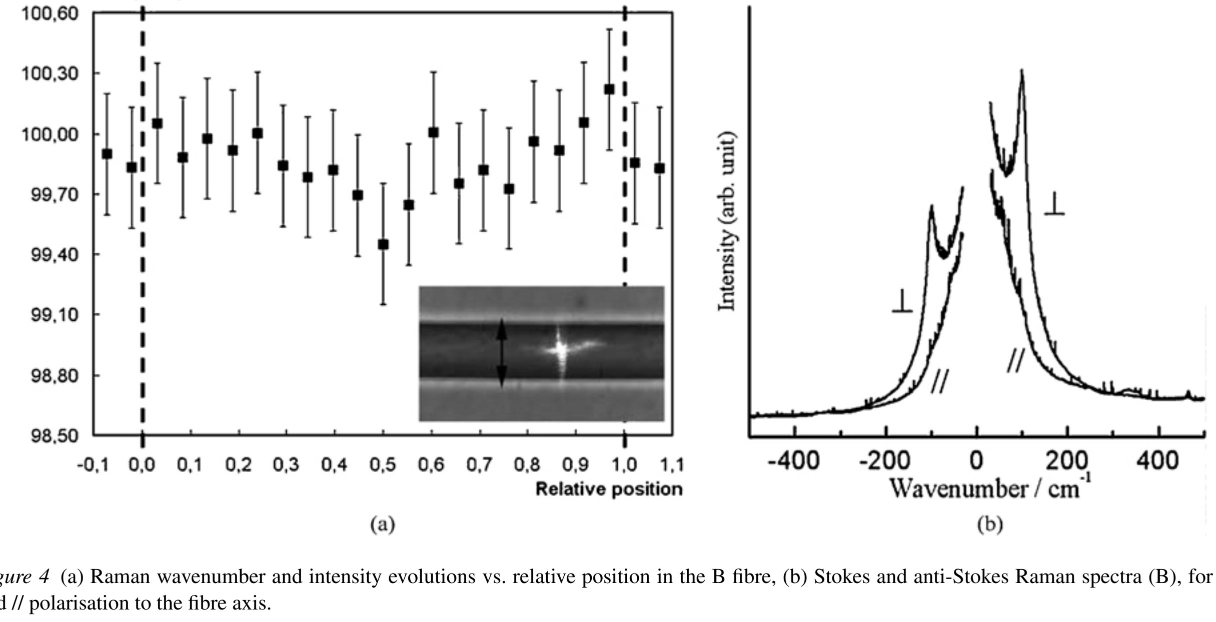

(a)

(b)

Figure 4 (a) Raman wavenumber and intensity evolutions vs. relative position in the B fibre, (b) Stokes and anti-Stokes Raman spectra (B), for ⊥ and // polarisation to the fibre axis.

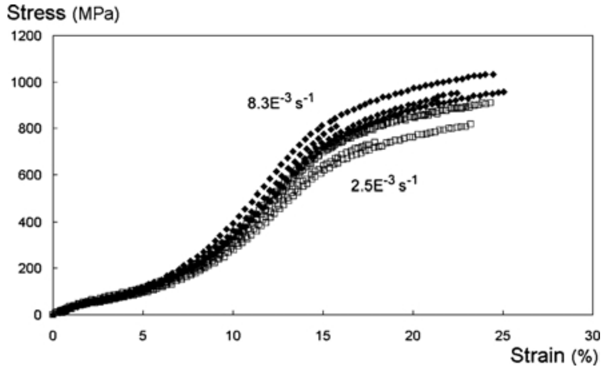

Figure 5 Typical stress-strain curves for two strain rates (♦) 8.3 E^{-3} s^{-1}, (□) 2.5 E^{-3} s^{-1} (sample A).

a damaged zone, a large wavenumber decrease ($\Delta \cong 2.5\ \text{cm}^{-1}$) of the band at 100 cm^{-1} was seen, corresponding locally to a high increase of tensile stress of about 2 GPa. Stress concentrations were seen at different points along the fibre.

3.3. Micro/macro behaviour mechanisms and failure analysis

3.3.1. Mechanical behaviour and microstructural evolution during loading

Tensile tests were conducted at two strain rates $2.5 \times 10^{-3}\ \text{s}^{-1}$ and $8.3 \times 10^{-3}\ \text{s}^{-1}$. Typical stress-strain curves are shown Fig. 5 for both strain rates. Despite a systematic measurement of fibre diameter, (accuracy of $\pm 0.05\ \mu$m), it can be seen that there was considerable dispersion of the mechanical behaviour. The progressive stiffening of the fibre during loading is interpreted as being entropic or rubber-like behaviour, the progressive alignment of molecules producing an increase in stiffness. Moreover, the large strain rate dependence reveals the viscoelastic component of the mechanical behaviour which depends on the amorphous domains.

Microstructural evolution during loading was studied by WAXD. Measurements were performed at three strain levels (0%, 5% and 10%) for sample B. Tests were run after stabilisation of mechanical behaviour. Results are summarized in Table II.

Two important stages can be seen in the behaviour. Initially, the amorphous domains accommodate the deformation. The *Foa* greatly increases up to 5% strain. In this strain range a large part of isotropic amorphous region becomes aligned (*Xia*) and amorphous orientation gradually increases from 0 to 10%. In a second step, for higher strain rates (over 5%), then crystalline orientation evolution occur. The ACS_{100}, relatively constant from 0% to 5%, was seen to decrease at 10% involving lamella damage in the hydrogen bonding direction (disruption or distortions of the unit cells along the crystallographic direction **a**). The interlayer distance d_{100} also decreased with loading which implies a load transfer into covalent chains of the crystal.

TABLE II Microstructural evolution during loading, at 0%, 5% and 10% of strain level

Fibre B	0%	5%	10%
α_I%	83	81	74
Xc%	46	52	53
Xia%	31	25	24
Foa	0.42	0.47	0.49
f_c	0.977	0.974	0.983
f_{am}	0.655	0.691	0.718
ACS_{100} (Å)	66	66	57
$2d_{100}$ (Å)	4.36	4.33	4.32

In the **b** direction (Van der Waals interaction direction), it was very difficult to interpret the (010) contribution from the (110) layers because of the important overlapping of these peak. Moreover, no significant variation of position and fwhm of (010 + 110) peak was seen.

An increase of crystallinity was noted together with the stabilisation of the *Xoa* values. Orientation of the amorphous phase seems to contribute to the growth of crystalline regions in the [010] direction and to the evolution of *Xia* into *Xoa*.

Birefringence measurements of samples loaded to failure were performed to study the reversibility of the behaviour. The results show a slightly irreversibility of microstructure after failure. The greater the sample is disoriented the more the residual increase of birefringence is marked: from +0.1 for sample B, to +0.9 sample A and to +1.4 for sample C. This effect is not only due to the amount of isotropic amorphous regions present in the fibre, because samples A and C have shown the same *Xia*, but is caused by the orientation potential of the different domains. Important changes in f_c and f_{am} are observed during the mechanical loading.

3.3.2. Probabilistic failure analysis

SEM observations of tensile breaks always showed the same morphology: a crack initiation near the surface followed by stable crack growth and finally unstable crack propagation. Weibull statistics were used to analyse the tensile results with a minimum of 30 specimens tested. The Weibull model gives P, probability density of fracture:

$$P(\sigma \geq \sigma_R) = 1 - \exp\left(-\left(\frac{\sigma}{\sigma_{0^*}}\right)^{m^*}\right) \tag{7}$$

in which the Weibull's modulus m^* characterises dispersion of critical size of defect and σ_{0^*} characteristic strength. This model is based on weakest-link theory which implies brittle fracture.

Fracture toughness is defined as the critical stress intensity factor:

$$K_{IC} = Y\sigma_c\sqrt{\pi a_c} \tag{8}$$

in which Y is the shape factor, σ_c the critical stress and a_c the critical crack size.

Crack morphology of PA 66 fibres clearly shows stable crack growth. In order to apply a time-dependent Weibull's model (4), a stable crack propagation law

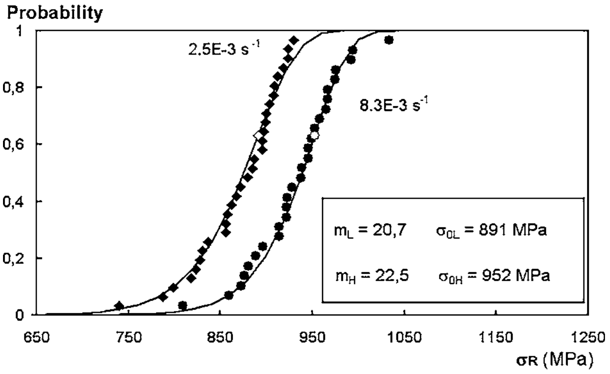

Figure 6 Statistical Weibull's treatment, results for both strain rates (sample A).

such as Evans law is introduced [12]:

$$\frac{\mathrm{d}a}{\mathrm{d}t} = \mathrm{A}K_{\mathrm{I}}^{n} \tag{9}$$

with A a shape parameter and K_{I} stress intensity factor.

$$P(\sigma \geq \sigma_{\mathrm{R}}) = 1 - \exp\left(-\left(\frac{\sigma}{\sigma_0}\right)^{m}\right) \tag{10}$$

Fig. 6 represents the application of the model for both strain rates. The model seems adapted to the analysis of fibre rupture. Dispersion of critical defect sizes is in both cases quite similar. However, the strain rates effect take into account on the scale factor σ_0.

$$\sigma_{0\mathrm{L}} = 891 \text{ MPa (low strain rate)}$$

$$\sigma_{0\mathrm{H}} = 952 \text{ MPa (high strain rate)}$$

From Equations 7–10 it is possible to correlate σ_0 and σ_{0^*} as follows:

$$\frac{\sigma_{0^*}}{\sigma_0} = \left(\frac{AY^2\pi}{2}\right)^{\frac{1}{n-2}} K_{\mathrm{IC}} t^{\frac{1}{n-2}} \tag{11}$$

In our case $n \gg 1$ and $m \cong m^*$ and finally:

$$\sigma_0 t^{\frac{1}{n-2}} = \text{constant} \tag{12}$$

Evaluating the size of the defect (stable propagation zone) the fracture toughness K_{IC} in case of high strain rate, has been determined. This calculation was done for 2 samples:

A: $K_{\mathrm{IC}} \cong 170 \text{ MPa} \cdot \text{mm}^{1/2}$ (i.e., $F_{\mathrm{R}} \cong 86.5$ cN/tex)

B: $K_{\mathrm{IC}} \cong 180 \text{ MPa} \cdot \text{mm}^{1/2}$ (i.e., $F_{\mathrm{R}} \cong 92.0$ cN/tex).

That way, the critical defect size is considered to be the size of stable crack growth zone, assuming then that failure is totally brittle.

4. Conclusions

The main roles played by the amorphous domains and crystallites have been studied by WAXD and show the important contribution of the amorphous phase below 5% strain. The mechanical behaviour showed also a large dependence on strain rate due to the viscoelastic behaviour of the amorphous regions. The use of a probabilistic treatment of tensile failure for both strain rates shows the applicability of using Weibull model to the failure of PA 66 fibres. Moreover, introducing a stable crack propagation law to the Weibull's theory, an analytical evaluation of the fibre strength has been obtained and is in quite good agreement with respect to the experimental data. The existence of a property gradient in the fibre section has been demonstrated by μ-Raman spectroscopy. This skin/core effect varies along the fibre and residual compression stresses of about 200 MPa in skin have been revealed. The first few microns of the fibre surface experience different strains from the core of the fibre.

Acknowledgements

The authors wish to thank Rhodia for the supply of fibres, for their financial support and Dr. L. Nasri (Rhodia-Industrial Yarns, Swiss) and Dr. G. Robert (Rhodia-CRL, France) for their close collaboration in this study; Mr D. Pachoutinsky and Mr Y. Favry for XRD technical assistance and discussion; Mr G. Sagon for Raman measurements and Mr Ph. Menez for birefringence measurements.

References

1. N. S. MURTHY and H. MINOR, *Polymer* **36** (1995) 2499.
2. A. PONNOURADJOU, Thèse, Ecole Nationale Supérieure des Mines de Paris (1998).
3. R. S. STEIN and F. H. NORRIS, *J. Polym. Sci.* **21** (1956) 381.
4. G. T. DAVIS and H. S.TAYLOR, *Text. Res. J.* **35** (1965) 405.
5. M. F. CULPIN and K. W. KEMP, *Proc. Phys. Soc.* **69** (1957) 1301.
6. M. INOUE, *J. Polym. Sci.* **1** (1963) 2697.
7. A. R. BUNSELL, J. W. S. HEARLE and R. D. HUNTER, *J. Phys.* E **4** (1971) 868.
8. C. W. BUNN and E. V. GARNER, *Proc. R. Soc. Lond.* A **189** (1947) 39.
9. H. HABERKORN, K. H. ILLERS and P. SIMAK, *Polym. Bull.* **1** (1979) 485.
10. H. W. STARKWEATHER, P. JR. ZOLLER and G. A. JONES, *J. Polym. Sci. Polym. Phys. Ed.* **22** (1984) 1615.
11. L. E. ALEXANDER, "X-ray Diffraction Methods in Polymer Science" (Wiley, New York, 1969) p. 241.
12. A. MARCELLAN, "Contribution à l'étude des Parametres Microstucturaux et des Propriétés Ultimes des Fibres de Polyamide 6.6." (Internal Report, Centre des Matériaux ENSMP, 2000) p. 32.

Received 7 August
and accepted 12 November 2002